Design of Hypervelocity-Impact Damage Assessment Technique based on Variational Bayesian

Haonan Zhang* Chun Yin* Xuegang Huang**
Sara Dadras*** Kai Chen* Soodeh Dadras*** Bing Zhu****

* *School of Automation Engineering, University of Electronic Science and Technology of China, Chengdu 611731, P. R. China (e-mail: yinchun.86416@163.com, chunyin@uestc.edu.cn).*
** *Hypervelocity Aerodynamics Institute, China Aerodynamics Research & Development Center, Mianyang 621000, P. R. China.*
*** *Electrical and Computer Engineering Department, Utah State University, Logan, UT 84321, USA.*
**** *Seventh Research Division, School of Automation Science and Electrical Engineering, Beihang University, Beijing, China.*

Abstract: In this paper, a damage assessment framework based on the infrared technology is proposed to assess the damage of the spacecraft. This framework mainly contains three steps. Firstly, a damage reconstruction model based on sparse model is proposed to reconstruct the damage image of different layers. To estimate the parameter of the model, variational Bayesian is used for calculating the parameters. Secondly, a damage extraction method is used to eliminate noise in the images. At the same time, this procedure can effectively make the weak subsurface damage more clear. Finally, in order to compare the location of surface and subsurface damage, image fusion method is used to achieve damage fusion. In the experiment, the proposed framework is used for the Whipple shield detection, both images and evaluation parameters show the effectiveness and high-accuracy of the new model.

Keywords: Damage reconstruction model, Variational Bayesian

1. INTRODUCTION

The spacecraft is one of the important tools for people to explore the space. However, the huge amount of space debris (Fang et al 2019) in hypervelocity have an immeasurable impact on the safe use of the spacecraft. Therefore, the assessment of the aerospace material damage becomes important. Infrared technology can be effectively used for damage extraction of spacecraft because it is non-contact, fast and convenient Huang et al. (2020). In the process of data acquisition, an infrared camera is used to record the thermal distribution of the material, and the collected data contain the different damaged information and non-damaged information (Maldague 2001), (Yin et al 2019). Due to the difference of the medium between the damaged areas and non-damaged areas, the heat distribution in different layers of damage may be different. These differences can be applied to reconstruct different layers of damage. In order to extract the characteristic of different layers of damage to reconstruct damage information. In (Gao et al 2001), a linear model is used to described the thermal images, and independent component analysis (ICA) (Chen et al 2018), principal Component Analysis (PCA) (Meng et al 2018) are used to reconstruct the damaged information. In (Fan et al 2019), Flourier transform and other methods are used to reconstruct the defects of the topography images.

In addition, the sparse models are rapidly developed in many fields. A multi-tasks sparsity model is applied to achieve human-machine interaction. (Sun et al 2019). In (Wang et al 2018), a joint sparse model based on cone, which replaces the infinite space of pixels with a non-negativity space of pixels, is used to classify the hyperspectral image. Currently, sparse model can be used to realize pattern recognition. In (Peng et al 2012), robust PCA is proposed to decompose linearly correlated images. Also, a multi-objective memetic algorithm is proposed to extract the sparse components of the images in (Wu et al 2018). In order to realize face recognition, a sparse corruption non-negative matrix factorization method is proposed in (Guo et al 2019). In (Yan et al 2017), a sparse model is proposed to reconstruct the ghost-free high dynamic range image. Cross-validation (CV) methods (Ward 2009), (Lingraj et al 2018), Markov chain Monte Carlo (MCMC) methods (Cai et al 2018), (Ginting et al 2015) and variational Bayesian method (Zhang et al 2015), (Qin et al 2019) can be used for sparse decomposition. Hence, they can be used to mine damaged information from infrared thermal image data.

In this paper, a damage assessment framework is proposed to realize the assessment of spacecraft. The main structure of the spacecraft is the Whipple shield structure (Zhang et al 2018). It is considered as a two-layer structure, which can improve the the protection level of the spacecraft and also can against hypervelocity impact of space debris. The main contributions of our works are as follows:

(1) A damage assessment framework is proposed to assess hypervelocity impact. It contains a damage reconstruction model and an image processing model;

(2) In the proposed method, it is the first time to reconstruct the damage image of hypervelocity impact by the variational Bayesian method;

(3) An image processing framework is proposed to process damage images of hypervelocity impact, which contains the image smoothing and segmentation based on mean shift algorithm (Zhang et al 2012), (Zhou et al 2013), and image fusion method based on multi-scale transform (He et al 2018), (Zhao et al 2019).

2. DAMAGE ASSESSMENT FRAMEWORK

Due to the complexity and diversity of the debris in the space, it can cause many different damages to the spacecraft. Directly observable damages such as craters and perforations may occur on the surface. It is also worth mentioning that there may be bulges, peelings and other damages in the invisible subsurface. To detect the damage, infrared technology is considered to be an effective technology, which achieves target recognition through the difference of heat between damaged area and non-damaged area. An infrared thermography damage detection system is shown in Fig. 1. A signal generator is used to generate the excitation signal, then the signal drives the flash excitation equipments on the material. After that, the light energy on the surface of the material is converted into heat energy. Finally, an infrared camera is used to record the heating process of material, and a series of recorded infrared images constitute an infrared image sequence.

The thermal image sequence can be described by a matrix block ($Y' \in R^{I \times J \times N_t}$), where the first two dimensions represent spatial information, and the last one represents time information. As shwon in Fig. 1, there is a lot of damage information in it. Hence, a detection framework is proposed to extract the damaged area in this paper. As shown in Fig. 2, this detection framework mainly includes three parts. Firstly, a damage reconstruction model is proposed to reconstruct the damage image. After that, an image processing framework for further processing of damage images is proposed, which includes two steps: a damage extraction method is used to eliminate noise and improve the clarity of subsurface damage. Also, a damage fusion method is applied to compare the damage of different layers.

3. PROPOSED METHOD

3.1 Establishment of model

In this Section a damage reconstruction model is proposed to reconstruct images of the damage. X_F, X_B and X_N are
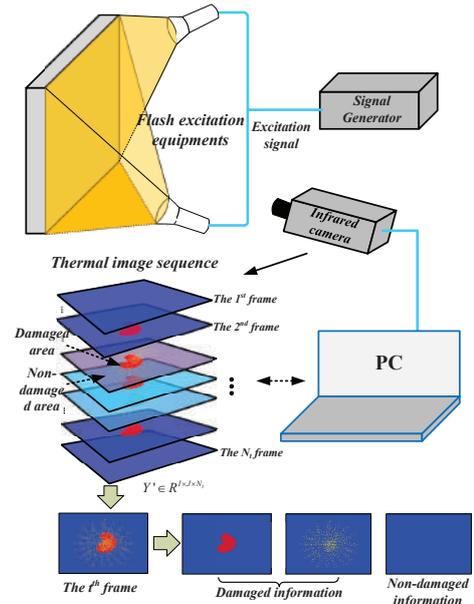
Fig. 1. Infrared thermography damage detection system.
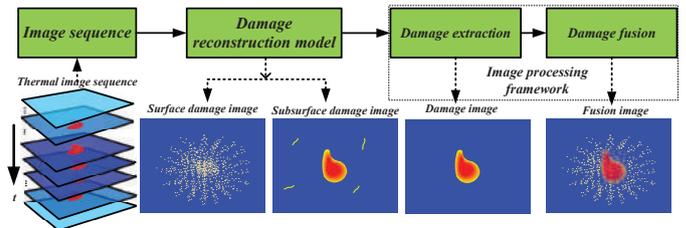
Fig. 2. Detection framework.

used to describe the characteristic of the damage on the surface, that of the damage on the subsurface and that of the non-damaged areas respectively. Then, the damage reconstruction model is as follows:

$$Y = \underbrace{\sum_{t_F=1}^{N_{t_F}} X_F(t_F)\lambda_F(t_F)}_{D_F} + \underbrace{\sum_{t_B=1}^{N_{t_B}} X_B(t_B)\lambda_B(t_B)}_{D_B}$$
$$+ \underbrace{\sum_{t_N=1}^{N_{t_N}} X_N(t_N)\lambda_N(t_N)}_{B} + N \qquad (1)$$

where $Y \in R^{K \times N_t}$, $K = I \times J$ is converted from Y', $Y = [vec(Y'(1)), vec(Y'(2)), ..., vec(Y'(N_t))]$, vec (Gao et al 2015) is the vectorization operator. $X_F \in R^{K \times N_{t_F}}$, $X_B \in R^{K \times N_{t_B}}$, $X_N \in R^{K \times N_{t_N}}$. $X_B(t_B)$, $X_F(t_F)$ and $X_N(t_N)$ are the columns vector of X_B, X_F and X_N respectively. $\lambda_F \in R^{N_{t_F} \times N_t}$, $\lambda_B \in R^{N_{t_B} \times N_t}$ and $\lambda_N \in R^{N_{t_N} \times N_t}$ represent their respective mixed parameter matrices, and $\lambda_F(t_F)$, $\lambda_B(t_B)$ and $\lambda_N(t_N)$ are the rows vector of λ_F, λ_B and λ_N respectively. N represents the noise matrix.

The low rank matrix B can be used to represent the linear combination of the non-damaged area. In addition, since the damage is only a small part of the overall material, the linear combination of surface damage and that of sub-surface damage can be expressed by sparse

matrices D_F, D_B respectively. Through the singular value decomposition (SVD), $B = ST^T$, where $S \in R^{K \times r}$, $T \in R^{N_t \times r}$. In order to calculate the sparse model, each column of S and T is set to obey the Gaussian distribution with mean of zero and precision of σ_j, the probability density functions are as follows: $p(S|\sigma) = \prod\limits_{j=1}^{r} N(s_j|0, \sigma_{\bullet j}^{-1} E_K)$, $p(T|\sigma) = \prod\limits_{j=1}^{r} N(t_j|0, \sigma_{\bullet j}^{-1} E_{N_t})$, where E is the unit matrix, σ_j obeys the Gamma distribution, i.e. $p(\sigma_i) = Gamma(u, \frac{1}{v}) \propto \sigma_i^{u-1} \exp(-v\sigma_i)$, where u and v are hyperparameters.

Each element of D_F and D_B obeys the Gaussian distribution with mean of zero and precision of α_{ij} and β_{ij} respectively, the probability density functions are as follows: $p(D_F|\alpha) = \prod\limits_{i}\prod\limits_{j} N(d_{F_{ij}}|0, \alpha_{ij}^{-1})$, $p(D_B|\beta) = \prod\limits_{i}\prod\limits_{j} N(d_{B_{ij}}|0, \beta_{ij}^{-1})$, where α_{ij} and β_{ij} obey Jeffrey's prior, i.e., $p(\alpha_{ij}) = (\alpha_{ij})^{-1}$, $p(\beta_{ij}) = (\beta_{ij})^{-1}$, $i = 1, 2, ..., K$, $j = 1, 2, ..., N_t$.

The noise is Gaussian noise and the probability density function is as follows: $p(N|\eta) = N(N|0, \eta^{-1} E_{KN_t})$, where $p(\eta) = \eta^{-1}$.

In (1), the conditional probability of the observed signal can be express as: $p(Y|S, T, D_F, D_B, \eta)$ $= \prod\limits_{i}\prod\limits_{j} N(Y|ST^T + D_F + D_B, \eta^{-1} E_{KN_t})$ and the joint probability of the model is as follows: $p(Y, S, T, D_F, D_B, \sigma, \alpha, \beta, \eta) = p(Y|S, T, D_F, D_B, \eta) p(S|\sigma) p(T|\sigma) p(D_F|\alpha) p(D_B|\beta) p(\sigma) p(\alpha) p(\beta) p(\eta)$

3.2 Estimation of Model Parameters

In this paper, variational Bayesian inference based on mean field theory (Qin et al 2019) is used to estimate parameters. The posterior probability of each hidden variable is calculated by minimizing KL divergence (Kullback et al 1951). In the joint probability, the set of variables is $Z = (S, T, D_F, D_B, \sigma, \alpha, \beta, \eta)$. Then, $Q(Z_k)$ is used to represent the posterior, $k = 1, ..., 8$, the estimation process is as follows:

$$\ln Q(Z_k) = \langle \ln p(Y, Z) \rangle_{Z \neq Z_k} + C \qquad (2)$$

where $\langle \bullet \rangle$ represents expectation, C is a constant, each hidden variable is independent of each other.

a) **Calculation of S and T:** Each row of S obeys the Gaussian distribution, the mean can be expressed as:

$$\langle s_{i\bullet} \rangle^T = \langle \eta \rangle \Sigma^S \langle T \rangle^T (y_{i\bullet} - d_{F_{i\bullet}} - d_{B_{i\bullet}})^T \qquad (3)$$

where $\Sigma^S = (\langle \eta \rangle \langle T^T T \rangle + \gamma)^{-1}$ represents variance of S. γ represents a matrix, which the diagonal is σ_j. $\gamma = diag(\sigma_1, ..., \sigma_r)$. In addition, each row of T obeys the Gaussian distribution and its mean can be expressed as:

$$\langle t_{j\bullet} \rangle^T = \langle \eta \rangle \Sigma^T \langle S \rangle^T (y_{\bullet j} - d_{F_{\bullet j}} - d_{B_{\bullet j}})^T \qquad (4)$$

where $\Sigma^T = (\langle \eta \rangle \langle S^T S \rangle + \gamma)^{-1}$ represents variance of T. Then, $B = \langle S \rangle \langle T \rangle^T$, it is used to represent non-danaged areas.

b) **Calculation of σ:** The posterior of σ_j is the Gamma distribution, the mean is as follow:

$$\langle \sigma_{\bullet j} \rangle = \frac{K + N_t + 2u}{\langle s_{\bullet j}^T s_{\bullet j} \rangle + \langle t_{\bullet j}^T t_{\bullet j} \rangle + 2v} \qquad (5)$$

where $\langle s_{\bullet j}^T s_{\bullet j} \rangle = \langle s_{\bullet j} \rangle^T \langle s_{\bullet j} \rangle + K(\Sigma^S)_{jj}$, $\langle t_{\bullet j}^T t_{\bullet j} \rangle = \langle t_{\bullet j} \rangle^T \langle t_{\bullet j} \rangle + N_t (\Sigma^T)_{jj}$.

c) **Calculation of D_F and D_B:** From (2), each element in D_F and D_B obeys Gaussian distribution, and their mean can be expressed as follows:

$$\langle d_{F_{ij}} \rangle = \frac{\langle \eta \rangle}{\langle \eta \rangle + \langle \alpha_{ij} \rangle} (y_{ij} - \langle s_{i\bullet} \rangle \langle t_{j\bullet} \rangle^T - \langle d_{B_{ij}} \rangle) \qquad (6)$$

$$\langle d_{B_{ij}} \rangle = \frac{\langle \eta \rangle}{\langle \eta \rangle + \langle \beta_{ij} \rangle} (y_{ij} - \langle s_{i\bullet} \rangle \langle t_{j\bullet} \rangle^T - \langle d_{F_{ij}} \rangle) \qquad (7)$$

d) **Calculation of α, β and η:** The posterior probabilities of α_{ij}, β_{ij} and η obey Gamma distribution, where each mean is as follows:

$$\langle \alpha_{ij} \rangle = \frac{1}{\langle d_{F_{ij}}^2 \rangle} = \frac{1}{\langle d_{F_{ij}} \rangle^2 + \Sigma_{ij}^{D_F}} \qquad (8)$$

$$\langle \beta_{ij} \rangle = \frac{1}{\langle d_{B_{ij}}^2 \rangle} = \frac{1}{\langle d_{B_{ij}} \rangle^2 + \Sigma_{ij}^{D_B}} \qquad (9)$$

$$\langle \eta \rangle = \frac{KN_t}{\langle \| Y - ST^T - D_F - D_B \|_F^2 \rangle} \qquad (10)$$

where $\left\langle \| Y - ST^T - D_F - D_B \|_F^2 \right\rangle = \left\| Y - \langle S \rangle \langle T \rangle^T - \langle D_F \rangle - \langle D_B \rangle \right\|_F^2 + Tr(N_t \langle S \rangle^T \langle S \rangle \Sigma^T) + Tr(K \langle T \rangle^T \langle T \rangle \Sigma^S) + Tr(KN_t \Sigma^S \Sigma^T) + \sum\limits_{i=1}^{K} \sum\limits_{j=1}^{N_t} \Sigma_{ij}^{D_F} + \sum\limits_{i=1}^{K} \sum\limits_{j=1}^{N_t} \Sigma_{ij}^{D_B}$. $Tr(\bullet)$ represents the trace of the matrix.

After initializing the parameters, the matrix of the model is obtained by optimizing the parameters by iteration (3), (4), (5), (6), (7), (8), (9) and (10). Finally, each column in D_F and D_B can be used to represent an image, and then the image S_F and S_B with the strongest color contrast between the damaged and non-damaged areas are selected to represent the damage information. By solving the damage reconstruction mode, the damage images of different areas can be obtained. However, data acquisition and model solving can add noise in the images. Hence, the damage images need to be further processed.

4. IMAGE PROCESSING FRAMEWORK

Damage in different layers can be described by reconstructed images. However, since noise can be added to the images in data acquisition and damage reconstruction, an image processing framework is proposed in this section to extract effective damaged areas and illustrate the location of subsurface damage. Firstly, mean-shift algorithm is used to extract effective damaged areas, the specific steps are as follows:

(A) $S = (s_s, s_c)$ is used to represent the image, in which s_s and s_c represent spatial and color information, respectively. When $k = 1$, initializing h_s and h_c, where h_s and h_c represent the size of spatial window and color window,

respectively. Also, initializing the minimum number of local pixels M.

(B) Update each pixel:

$$SS_i^{k+1} = \frac{\sum_{n=1}^{K} S_n G_{h_s,h_c}(S_n - SS_i^k)}{\sum_{n=1}^{K} G_{h_s,h_c}(S_n - SS_i^k)} \qquad (11)$$

where

$G_{h_s,h_c}(S_n - SS_i^k) = \frac{C}{h_s^2 h_c^3} g\left(\left\|\frac{s_n - ss_{i_s}^k}{h_s}\right\|\right) g\left(\left\|\frac{s_c - ss_{i_c}^k}{h_c}\right\|\right)$ is used to represent a kernel function, C is a constant.

(C) When $\left|SS_i^{k+1} - SS_i^k\right| < \varepsilon$, then $Z_i = (z_{i_s}, z_{i_c}) = SS_i^{k+1}$, otherwise $k = k + 1$ and return to Step (B).

(D) If the pixels satisfy $\|z_s - z_{i_s}\| < h_s$ and $\|z_c - z_{i_c}\| < h_c$, they are merged into the same category. Each category has Num_{C_q} pixels, where $q = 1, 2, ..., Q$. If $Num_{C_q} < M$, then combine the qth category and its neighborhoods. Q' is used to represent the number of final categories.

(E) Calculate the value of the ith pixel:

$$S_i^* = \{z_{i_c} | z_{i_c} = \sum_{z_{i_s} \in C_q} z_{i_c} \Big/ Num_{C_q}, \qquad (12)$$
$$q = 1, ..., Q', i = 1, ..., K\}$$

The effective damaged areas can be obtain by mean-shift algorithm. Moreover, in order to illustrate the location of subsurface damage, multi-scale transform is used to achieve image fusion. The details are as follows:

(a) $t = 1$, initializing color images $_lR_F^0 = S_F^*$, $_lR_B^0 = S_B^*$, low-pass filter f_l and high-pass filter f_h, the maximum number of transformation T, where S_F^* and S_B^* represent images of damage in different layers.

(b) The images are transformed along the row by f_l and f_h: $L_F^t(i,:) = _lR_F^{t-1}(i,:) * f_l$, $H_F^t(i,:) = _lR_F^{t-1}(i,:) * f_h$, $L_B^t(i,:) = _lR_B^{t-1}(i,:) * f_l$ and $H_B^t(i,:) = _lR_B^{t-1}(i,:) * f_h$. The transformed images are represented as: $LH_F^t = (L_F^t : H_F^t)$ and $LH_B^t = (L_B^t : H_B^t)$. Sampling LH_F^t and LH_B^t along the column, and images $^*LH_F^t$ and $^*LH_B^t$ can be obtained.

(c) The images are transformed along the column: $LHL_F^t(:,j) = {}^*LH_F^t(:,j) * f_l$, $LHH_F^t(:,j) = {}^*LH_F^t(:,j) * f_h$, $LHL_B^t(:,j) = {}^*LH_B^t(:,j) * f_l$ and $LHH_B^t(:,j) = {}^*LH_B^t(:,j) * f_h$ to obtain $LHLH_F^t = \left(LHL_F^{t\,T} : LHH_F^{t\,T}\right)^T$ and $LHLH_B^t = \left(LHL_B^{t\,T} : LHH_B^{t\,T}\right)^T$. Down-sampling $LHLH_F^t$ and $LHLH_B^t$, $^*LHLH_F^t$ and $^*LHLH_B^t$ can be obtained, which include a part of the color image $_lR_F^t$, $_lR_B^t$ and three parts of the texture image $_hR_F^t$, $_hR_B^t$, respectively, where $_lR_\bullet^t$ represents the color image, which is initialized by the reconstructed image, $L_\bullet^t(i,:)$ and $H_\bullet^t(i,:)$ represent color and texture images along the row, respectively, and $LHL_\bullet^t(:,j)$, $LHH_\bullet^t(:,j)$ represent color and texture images along the column, respectively.

(d) $t = t + 1$, until $t > T$, otherwise return to Step (b).

(e) $tt = T$, initializing $_lR^T = a \cdot {}_lR_F^{tt} + b \cdot {}_lR_B^{tt}$, where $_lR^{tt}$ represents the fused color image, a and b represent fusion coefficients, $a + b = 1$.

(f) $_hR^{tt} = \max\{_hR_F^{tt}, {}_hR_B^{tt}\}$, where $_hR^{tt}$ represents fused the fused texture image. $_hR^{tt}$ and $_lR^{tt}$ form an image R^{tt}.

(a) The surface.   (b) The sub-surface.
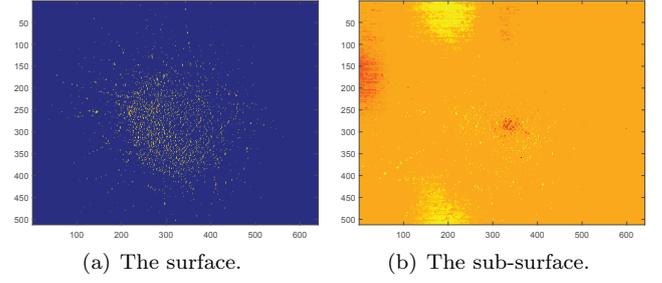
Fig. 3. The results of new method.

(g) Up-sampling R^{tt} to get $^*R_{col}^{tt}$. Then, transform it along the column $R_{cl1}^{tt} = {}^*R_{col}^{tt}(:,j) * \overline{f_l}$, $R_{cl2}^{tt} = {}^*R_{col}^{tt}(:,j) * \overline{f_h}$ to get an image R_{cl}^{tt}, where $\overline{f_l}$ and $\overline{f_h}$ represent inverse transformation; After that, up-sampling R_{cl}^{tt} to get $^*R_{row}^{tt}$. Then, transform it along the row $_lR_1^{tt} = {}^*R_{row}^{tt}(:,j) * \overline{f_l}$, $_lR_2^{tt} = {}^*R_{row}^{tt}(:,j) * \overline{f_h}$. Finally, $_lR_1^{tt}$ and $_lR_2^{tt}$ form an image $_lR^{tt-1}$.

(h) $tt = tt - 1$, until $tt < 1$, the final fused image is expressed $R = {}_lR^0$, otherwise, return to Step (f).

Finally, fusion image is obtained. It can be used to illustrate the location of subsurface damage, and analyse damage degree of materials.

5. SIMULATION AND EXPERIMENTAL RESULTS

The specimen to be tested in this paper is the rear wall of the Whipple shield at the impact velocity of 5.3 km/s. No perforation is found by direct observation even though there are pits on the surface, while peeling damage has been formed in the middle of the subsurface. In the experimental setup stage, the flash excitation equipments ares 5cm away from the material, and the infrared camera (made by FLIR) is 80cm away from the material. In the processing of data acquisition, setting the maximum power of Easyheat as 2.4KW, the maximum current is 400A, and the sampling frequency is 50Hz, the heating time is 8s. Finally, the collected infrared image sequence can be described by a $512 \times 640 \times 544$ matrix block.

Before the variational Bayesian process, since there is a lot of redundant information in the image sequence, PCA is used to extract effective frames with 95% importance. After that, variational Bayesian is used to reconstruct images of damage from model. Setting maximum number of iteration to 100 times. Also, hyperparameters u and v are set to 10^{-6}. Then, damage of different layers are shown in Fig. 3.

Fig. 3(a) shows the damage on the surface, through the comparison of Fig. 3(a) and Fig. ??, the result shows that the new method appear as granular in the figure, which can clearly describe the damage. In addition, Fig. 3(b) shows the damage on the subsurface, through the comparison of Fig. 3(b) and Fig. ??, there is a highlight part in the result of proposed method, which can accurately describe the peeling damage on the subsurface.

In total, the proposed model can both reconstruct the observable and unobservable damages on the surface and subsurface respectively. It is an effective method to assess the damage of the hypervelocity impact.
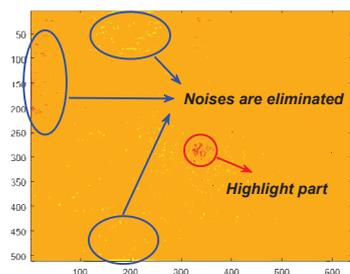
Fig. 4. The result of mean-shift.
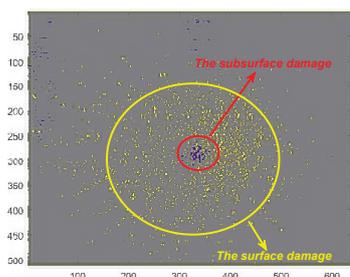
Fig. 5. The result of fusion.

As shown in Fig. 3(b), although the highlighted part can explain the damage on the subsurface, there is still weak interference information around it. Therefore, the mean-shift method is used to process the images. The kernel function is set to Gaussian function, where $h_s = 6$ and $h_c = 6$. Also, The minimum number of local pixels is set to $M = 9$, termination condition is set to $\varepsilon = 0.01$. Then, the results are shown in Fig. 4. In Fig. 3(b), there are two yellow bright spots on the upper and lower edges of the image, and another red bright spot is on the left edge. These bright spots are noises formed in the process of damage reconstruction and data acquisition. However, the bright spots at different positions are eliminated in Fig. 4, also the image only highlights the subsurface damage in the middle. That means the redundant information is removed by mean-shift method.

Then, to visually explain the damages of the spacecraft, the image shown in Fig. 3(a) and Fig. 4 are fused by a fusion method. Setting $f_l = [1, 1]$, $f_h = [1, -1]$, $T = 2$, fusion coefficients are set to $(a = 0.3, b = 0.7)$. Finally, the result is shown in Fig. 5. The red part in the middle is the unobservable damage on the subsurface, and the yellow spot around it is the pit damage on the surface.

The images of each step of the proposed method illustrate our method can be used to assess the damage of hypervelocity impact. Moreover, to objectively evaluate proposed method, F-score and accuracy are used to describe the performance of the method. In the evaluation process, an infrared camera is used to collect the infrared photos of the surface and subsurface of the material to form a comparative standard image. After that, selecting a frames containing the respective damage from image sequences respectively. As show in Fig. 6(a), image i represents the image selected from the image sequence of surface of the material, and Fig. 6(b) is considered as the image selected from the image sequence of subsurface of the material. Then marking different areas of the image, as shown in Fig. 6, Event 1 represents subsurface damaged area, event

(a) Image i.

(b) Image ii.
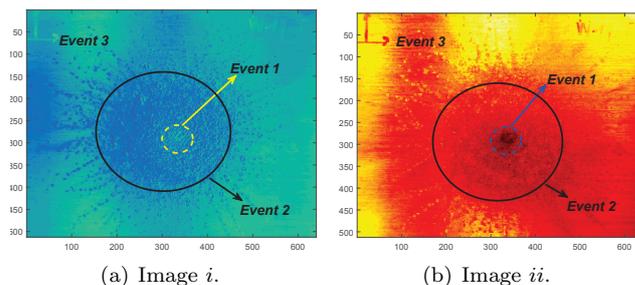
Fig. 6. Standard image.

2 represents surface damaged area and event 3 represents non-damaged area. After that, F-score and accuracy are used to illustrate the performance of the proposed method. The formulas are shown in appendix and parameters are shown in Table 1, the F-score of the proposed method is 1 and the accuracy is 100 %.

Table 1. Performance evaluation of the proposed method.

	TP	TN	FP	FN	F-score	Accuracy
Surface	1	2	0	0	1	100 %
Subsurface	1	2	0	0	1	100 %

In addition, the surface damage is clearly reconstructed by comparing Fig. 3(a) and Fig. 6(a). Also, by comparing Fig. 3(b) and Fig. 6(b), the result shows that the heat diffusion caused by the surface damage around the subsurface damage is removed. The highlighted area in the center is used to represent subsurface damage. These illustrate that our proposed method can effectively assess the surface damage and subsurface damage of the hypervelocity impact.

6. CONCLUSION

This paper illustrates a damage assessment framework for hypervelocity impact. The proposed method contains three parts. To start with, a damage reconstruction model is used to extract damage from image sequence. Moreover, mean-shift method is used to process images to, describe the damage more clear. Finally, an image fusion method is used to fuse damage images of different layers to visualize subsurface damage. In the experiment, the model is used to detect the damage of the rear wall of the Whipple shield. The effectiveness and accuracy of the model are illustrated intuitively through images. In addition, the F-score of the new method is 1.00 and the accuracy is 100%, which objectively shows that the model can be used for damaged information reconstruction.

REFERENCES

Yingwu Fang. Effects of space-based nanosecond pulse laser driving centimeter-sized space debris in LEO[J]. *Optik*, 2019, 185:12-17.

X. Huang, C. Yin, H. Ru, S. Zhao, Y. Deng, Y. Guo, and S. Liu, (2020). Hypervelocity impact damage behavior of B4C/Al composite for MMOD shielding application. *Materials & Design*, 186, 108323.

X.P. Maldague. Theory and practice of infrared technology for nondestructive testing, *John Wiley&Sons*, New York, 2001.

C. Yin, T. Xue, X. Huang, Y. Cheng, S. Dadras, and S. Dadras, (2019). Research on damages evaluation method with multi-objective feature extraction optimization scheme for M/OD impact risk assessment[J]. *IEEE Access*, 7, 98530 – 98545.

B. Gao, W.L. Woo, G.Y. Tian. Electromagnetic thermography nondestructive evaluation: physics-based modeling and pattern mining[J]. *Scientific Reports*, 2016, 6:25480.

Y. Chen, L.L. Niu, R.B. Chen, et al. Sparse-group independent component analysis with application to yield curves prediction[J]. *Computational Statistics & Data Analysis*, 2018. 63(4):913-922.

Z.Q. Meng, H. Shen, H.M. Huang, et al. Search result diversification on attributed networks via nonnegative matrix factorization[J]. *Information Processing & Management*, 2018:S0306457318300578-.

X.G. Fan, X.D. Wang. Image processing for three defects of topography images by SPM[J]. *Chemometrics and Intelligent Laboratory Systems*, 2019, 185:12-17.

J. Sun, Q.D Chen, J.N. Sun. Graph-structured multitask sparsity model for visual tracking[J]. *Information Sciences*, 2019.(486):133-147.

Z.Y. Wang, R. Zhu, K. Fukui. Cone-based joint sparse modelling for hyperspectral image classification[J]. *Signal Processing*, 2018, 144:417-429.

Y. Peng, A. Ganesh, J. Wright, W. Xu, and Y. Ma. RASL: Robust alignment by sparse and low-rank decomposition for linearly correlated images. *IEEE Trans. Pattern Anal. Mach. Intell.*, vol. 34, no. 11, pp. 2233C2246, Nov. 2012.

T. Wu, J. Shi, X.M. Jiang, et al. A multi-objective memetic algorithm for low rank and sparse matrix decomposition[J]. *Information Sciences*, 2018:S002002551830642X-.

Z.B. Guo, Y. Zhang. A Sparse Corruption non-negative natrix factorization method and application in face image processing & recognition[J]. *Measurement*, 2019, 136:429-437.

Q.S. Yan, J.Q. Sun, H.S. Li, et al. High dynamic range imaging by sparse representation[J]. *Neurocomputing*, 2017:S0925231217310020.

R. Ward. Compressed sensing with cross validation[J]. *IEEE Transactions on Information Theory*, 2009, 55(12):5773-5782.

D. Lingraj, A. Sanjay, P. Rutuparna, et al. Nested cross-validation based adaptive sparse representation algorithm and its application to pathological brain classification[J]. *Expert Systems with Applications*, 2018:S0957417418304627-.

C.F. Cai, et al. Metamodel-based Markov-Chain-Monte-Carlo parameter inversion applied in eddy current flaw characterization[J]. *NDT & E International*, 2018, 99:13-22.

V. Ginting, F. Pereira, A. Rahunanthan, et al. Multiphysics Markov-Chain-Monte-Carlo methods for subsurface flows[J]. *Mathematics & Computers in Simulation*, 2015, 118(C):224-238.

G.C. Zhang, N. Kingsbury. Variational Bayesian image restoration with group-sparse modeling of wavelet coefficients[M]. *Academic Press*, Inc. 2015.

L. Qin, Z. Wang, Q.J. Guan, et al. Variational Bayesian image restoration with multi-structured model

of wavelet transform coefficients[J]. *Signal Processing: Image Communication*, 2019, 72:1-8.

P.L. Zhang, et al. Study of the shielding performance of a Whipple shield enhanced by Ti-Al-nylon impedance-graded materials. *International Journal of Impact Engineering*, 2018:S0734743X18302872-.

S. Zhang, Y.P. Q. Mean-shift algorithm apply for infrared imaging tracking. *AASRI Procedia*, 1.Complete(2012):52-57.

H.Y. Zhou, X.L. Li, G. Schaefer, et al. Mean shift based gradient vector flow for image segmentation[J]. *Computer Vision and Image Understanding*, 2013, 117(9):1004-1016.

K.J. He, D.M. Zhou, X.J. Zhang, et al. Multi-focus: Focused region finding and multi-scale transform for image fusion[J]. *Neurocomputing*, 2018, 320:157-170.

D. Zhao, X. Long, et al. Multi-scale Optimal Fusion model for single image dehazing[J]. *Signal Processing: Image Communication*, 2019.74:253-265.

B. Gao, W.L. Woo, Y. He, et al. Unsupervised sparse pattern diagnostic of defects with inductive thermography imaging system[J]. *IEEE Transactions on Industrial Informatics*, 2015, 12(1).

S. Kullback, R.A. Leibler. On Information and sufficiency[J]. *Annals of Mathematical Statistics*, 1951

Appendix A. PERFORMANCE EVALUATION PARAMETERS

The F-score and accuracy are used to evaluate the performance, namely $F = \frac{2 \times macro.P \times macro.R}{macro.P + macro.R}$, $Accuracy = \frac{TP+TN}{TP+TN+FN+FP}$, where $macro.P = \sum_{i=1}^{n} P_i/n$, $macro.R = \sum_{i=1}^{n} R_i/n$, $P = TP/(TP + FP)$, $R = TP/(TP + FN)$. True positive (TP) represents area belonging to damaged area correctly predicted as belonging to the damaged area. True negative (TN) represents area correctly predicted as belonging to the non-damaged area. False positive (FP) represents area predicted as non-damaged area which real belongs to damaged area. False negative (FN) represent area predicted as damaged area which comes from non-damaged area.